Journal of Materials Chemistry C

ROYAL SOCIETY OF CHEMISTRY

PAPER

View Article Online
View Journal | View Issue

Cite this: J. Mater. Chem. C, 2023, 11, 12764

Chiral and conductive viologen-based supramolecular gels exhibiting tunable charge-transfer properties†

Vivien Andrieux, [a] Thomas Gibaud, *[b] Julien Bauland, [b] Thibaut Divoux, [b] Sébastien Manneville, [bd] Stéphan Guy, [c] Amina Bensalah-Ledoux, [c] Laure Guy, [a] Floris Chevallier, [a] Denis Frath *[a] and Christophe Bucher *[a]

Received 14th June 2023,
Accepted 24th August 2023

DOI: 10.1039/d3tc02076b

rsc.li/materials-c

Redox-active conductive supramolecular gels involving highly ordered chiral assemblies of small organic molecules are very promising soft materials for many applications ranging from catalysis to electronics. However, combining all these properties in the same material has so far remained a difficult task. We now report the synthesis and detailed structural, rheological, and electrical characterizations of supramolecular gels obtained by self-assembly of a dicationic low molecular weight gelator incorporating a redox-active 4,4′-bipyridinium unit. These molecules have been shown to self-assemble in pentanol to form chiral hollow core–shell cylinders, eventually yielding dendritic clusters inducing gelation. We also showed that the optical, rheological, and electrical properties of the gels can be tuned by adding ionic additives. Careful control of the formation of charge-transfer complexes between viologens and iodides has led to the formation of robust, transparent, conductive, and chiral gel. The gelation process, the properties of the gel, and the structure of the assemblies have been thoroughly investigated by UV-Vis and ECD spectroscopy, rheometry, bright-field microscopy, SAXS, AFM, electrochemical and impedance measurements.

Introduction

Supramolecular gels obtained through self-assembly of low molecular-weight gelators (LMWGs) have attracted increasing attention over the past decades.[1,2] It is now well recognized that the outstanding properties of those materials stem from the dynamic nature of the "weak bonds" involved in the 3D network leading to gelation, including hydrogen bonds, electrostatic/van der Waals forces, donor/acceptor interactions or metal–ligand bonds. Such gels built from reversible bonds are in fact ideally suited to developing stimuli-responsive materials capable of achieving drastic changes in shape, appearance, and rheological properties or of undergoing phase transitions in response to external stimuli.[3–6] Such responsiveness to different chemical or physical stimulations has, for instance, already proved useful in catalysis, or to the development of sensors, actuators, memory devices and smart material, as well as for pollutant removal or to regulate drug delivery and adhesion.[7–12] Pressure, light, sound, and pH are the most common stimuli used so far to trigger changes in the aggregation modes of molecular gelators, eventually leading to macroscopic changes.[3–6] Electrical stimulation has conversely received very little attention due to major scientific or technical locks associated with conceptualization and technical issues, the most important ones being the conductivity of the materials and the need to incorporate dedicated electron-responsive units. Two main types of supramolecular conductive gels have already been described in the literature. Examples of metal–organic gels (metallogels)[11–15] have been reported, eventually exhibiting both electronic and ionic conductivities thanks to the presence of redox-active metal center and of mobile counter ions,[16–18] as well as a substantial number of supramolecular gel electrolytes obtained from mixtures of redox-inactive salts and LMWGs.[19] The growing interest in conductive gels also comes from their numerous advantages over liquid electrolytes, including limited evaporation/leaking and flammability, and over polymeric electrolytes, with improved processability, recyclability, lifetime, and electric contact with electrodes.[20] Such conductive soft materials thus hold great promises in many different fields, such as for the development of solid electrolytes

[a] ENSL, CNRS, Laboratoire de Chimie UMR 5182, 46 allée d'Italie, 69364 Lyon, France. E-mail: denis.frath@ens-lyon.fr, christophe.bucher@ens-lyon.fr
[b] ENSL, CNRS, Laboratoire de Physique UMR 5672, 46 allée d'Italie, 69364 Lyon, France. E-mail: thomas.gibaud@ens-lyon.fr
[c] Univ. Lyon, Université Claude Bernard Lyon 1, CNRS, UMR 5306, Institut Lumière Matière, 69622, Lyon, France
[d] Institut Universitaire de France (IUF), Lyon, France

† Electronic supplementary information (ESI) available. See DOI: https://doi.org/10.1039/d3tc02076b

for lithium batteries,[21,22] dye-sensitized solar cells,[23,24] electromechanical actuators,[25] capacitors,[20,26] and conductive lubricant.[27]

We have focused in recent years on the development of supramolecular gels built from LMWGs incorporating 4,4′-bipyridinium units.[28–30] These planar dicationic π-conjugated acceptors, better known as viologens (V^{2+}), offer many advantages for developing conductive gels and hybrid materials.[31] In addition to providing two mobile counter anions, they can potentially participate in electron transport through two successive one-electron reductions yielding stable radical cations ($V^{+\bullet}$) and quinoid neutral species (V^0). These electron-responsive properties have already been extensively exploited for developing molecular machines or electrochromic devices and organic batteries.[32,33] Recently, viologens have also been used as redox-active units promoting charge transport in single molecule[34,35] and large-area molecular junctions.[36,37]

Despite their undeniable advantages, only a limited number of gels obtained from viologen-based LMWG can be found in the literature. Most reported viologen-based gels have been obtained in water upon exploiting the ability of viologens to form charge-transfer (CT) complexes with organic π-donor molecules.[38–40] These self-assemblies have, for instance, been used to produce self-erasing or thermochromic inks.[41,42] Viologen-based LMWGs have also been obtained by introducing various self-assembling functions promoting metal–ligand bonds,[28–30] H-bonds,[43] Coulombic forces[44] or van der Waals interactions.[45]

The ability of the cholesteryl substituted viologen derivative $\mathbf{1}^{2+}$ (Scheme 1) studied in the present article to form gels was first reported by Lu and coworkers.[45] In particular, the authors have shown that this LMWG can be used to form mesoporous silica fibers. Most studies have been however conducted on xerogels, while very little attention has been given to the gelation process itself and to the rheological and electrical properties of the gel state.

We now report detailed characterizations of the gels formed by self-assembly of $\mathbf{1}^{2+}$ in pentanol and show that the optical, rheological, and electrical properties of the gels can be tuned by the addition of ionic additives. The gelation process and the gel structure have been thoroughly investigated by UV-Vis and ECD spectroscopy, rheometry, bright-field microscopy, SAXS, and AFM measurements. The properties of the gels were characterized by rheometry, electrochemical impedance spectroscopy (EIS), and by electrochemical methods. Our results demonstrate that the ionic composition of the gel can be easily tuned to afford a wide range of robust, transparent, conductive, and chiral gels.

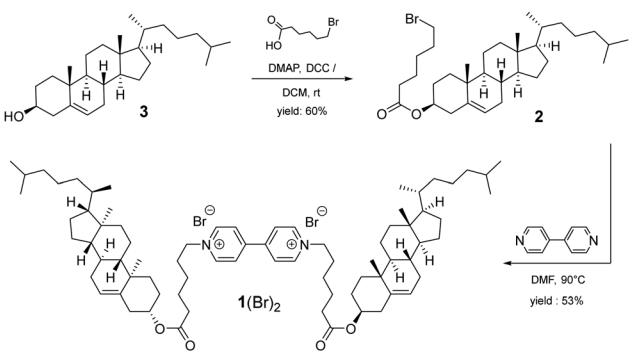

Scheme 1 Synthesis of $\mathbf{1}(Br)_2$.

Experimental

Synthetic procedures

All the commercially available compounds were used as received. 1-Pentanol (>99% pure), tetra-*n*-butylammonium bromide (>99%), and octanol (spectroscopic grade) were purchased from Sigma Aldrich. 4-Dimethylaminopyridine (>99%), dicyclohexylcarbodiimide (>99%), 1-butanol (>99%), extra dry DMF, lithium bis(trifluoromethylsulfonyl)imide (>99%) were purchased from Acros Organics. 4-4′-Bipyridyl (>98%) and bromohexanoic acid (>98%) were purchased from TCI. Cholesterol (>99%) was purchased from Fisher Chemicals. Dichloromethane (>99% pure, amylene stabilized) was purchased from Carlo Erba. Hexanol (>98%) was purchased from Fluka, and heptanol (>98%) from Amilabo. ^{1}H NMR spectra was recorded at room temperature in deuterated solvents ($CDCl_3$ and DMSO-d_6) on Bruker Advance 300 MHz or 400 MHz spectrometers available at ENSL. Chemical shifts were referenced to residual solvent peaks. Mass spectrometry measurements were carried out at the mass spectrometry facility of Lyon1 (CCSM) on a MicrOTOFQ II (Bruker) using the electrospray ionization (ESI) method.

The experimental procedures used to synthesize the targeted LMWG $\mathbf{1}^{2+}$ and its precursor **2** are detailed below. Both compounds are represented in Scheme 1.

Synthesis of 2. 6-Bromohexanoic acid (5.42 g, 27.8 mmol) and cholesterol (10.04 g, 25.9 mmol) were dissolved in 105 mL of dichloromethane under an argon atmosphere. To this solution, kept under stirring at 0 °C were added all at once dicyclohexylcarbodiimide (5.33 g, 25.8 mmol) and 4-dimethylaminopyridine (0.54 g, 2.58 mmol). The resulting mixture was stirred for 6 h at 0 °C and then for 16 h at room temperature. The white precipitate formed in solution was removed by filtration and the filtrate was washed three times with 40 mL of aqueous HCl (10%) and three times with saturated aqueous $NaHCO_3$. The organic phase was then dried using anhydrous sodium sulfate, filtered, and the solvent was removed under reduced pressure. The residue was purified by column chromatography on silica gel using ethyl acetate/petroleum ether (1 : 8, v/v) as an eluent. The targeted product **2** was obtained in 60% yield as a colorless solid. ^{1}H NMR (300 MHz, $CDCl_3$): δ = 5.37 (1H, d, J = 4.0 Hz), 4.64 (1H, m), 3.41 (2H, t, J = 6.7 Hz), 4.46 (4H, s), 2.30 (4H, m), 2.15-0.8 (47H, m), 0.65 (3H, s). HRMS (ESI-TOF): measured m/z = 585.3269 ($C_{33}H_{55}BrO_2Na^+$); calculated m/z = 585.3278.

Synthesis of $\mathbf{1(Br)_2}$. Compound **2** (1.52 g, 2.70 mmol), 4,4′-bipyridine (0.148 g, 0.95 mmol) and 25 mL of dry *N*,*N*-dimethylformamide were introduced in a 50 mL round bottom

flask equipped with a condenser connected to an oil bubbler. Stirring this mixture at 90 °C for 110 h under an argon atmosphere afforded a precipitate, which was filtered, washed with petroleum ether (4 × 10 mL), and dried under vacuum. **1**$(Br)_2$ was obtained as a pale-yellow solid in 53% yield. ^{1}H NMR (300 MHz DMSO-d_6): δ = 9.39 (4H, d, J = 6.9 Hz), 8.80 (4H, d, J = 6.9Hz), 5.35 (2H, unresolved signal), 4.69 (4H, t, J = 7.0 Hz), 4.40 (2H, m), 2.4–0.75 (97H, m), 0.65 (3H, s). HRMS (ESI-TOF): measured m/z = 561.4529 ($C_{76}H_{118}N_2O_4^{2+}$); calculated m/z = 561.4540.

Gel preparation

Gelation tests were conducted upon heating dispersions of **1**$(X)_2$ (X = Br^- or $TFSI^-$) in different solvents until complete dissolution. The targeted sol–gel transition was observed upon cooling. Careful control over the heating and cooling processes was achieved by applying programmable temperature ramps using an ''Eppendorf Thermomix C'', and applying a stirring rate of 1500 rpm during the heating step. An oil bath was used only when temperatures above 100 °C were required to achieve solubilization. The ability of a given sample to form gels was first tested visually by the ''inversion'' method. An inversion test, consisting in turning the sample upside down, was considered successful if the sample did not flow as the vial was left inverted for 10 minutes or more. The resistance to shearing of the gel samples was tested by shearing them with a spatula for a few seconds. The resistance to shearing test was considered successful if the sample was still able to pass an inversion test after being sheared.

Materials and methods

Absorption spectroscopy. Absorption spectra were recorded with an MCS 601 UV-NIR Zeiss spectrophotometer operating in the 250 to 1000 nm range. Gel samples were heated until forming solutions which could then be easily poured in a 1 mm quartz cuvette. The reversible Sol↔Gel transition could then be followed by performing heating and cooling cycles. The gelation process was, for instance, studied after heating the cuvette up to the Gel → Sol phase transition temperature. The sample was then quickly placed in the spectrometer to record the evolution of the absorption spectra as a function of time at a rate of 0.5 Hz. Gelation was induced in this case by natural cooling of the sample down to room temperature (T = 20 °C).

Circular dichroism. UV absorption and CD measurements were recorded using a homemade setup allowing us to measure linear and circular dichroism data. Light polarization is modulated by means of a linear polarizer followed by the photoelastic modulator (PEM) driven at 50 kHz. The transmitted light from the sample is Fourier analyzed to get the CD and LD (Linear Dichroim) signals at 50 and 100 kHz, respectively. The main issue with CD measurement within non-isotropic materials is the possible linear contributions coming from LD and LB (Linear Birefringence) to the CD signal leading to possible misinterpretation. Thus, CD measurement of anisotropic samples requires special care. In particular, in the case of our gel samples, we first checked the possible existence of LD contribution by measuring the signal at 100 kHz and rotating the sample around the optical axis (perpendicularly to the light beam). This signal being always around 0 at 0° and 45°, we concluded that the samples present no LD and that the signals recorded at 50 kHz are purely CD ones. Using a 1 mm path length quartz cell, spectra were measured in the 200–500 nm wavelength range with a 1 nm increment and a 2s/step integration time. The evolution of CD during gelation process has been studied after heating the cuvette above the gel–sol transition temperature. The sample was then quickly placed in the spectrometer to record the evolution of the CD spectra in the 260–290 nm wavelength range as a function of time (2 nm increment, 2 s/step integration time). Gelation was induced in this case by natural cooling of the sample down to room temperature (*ca.* 25–30 °C).

Rheology. Rheological characterizations were performed with a stress-imposed rheometer (Anton Paar MCR301) using a smooth parallel-plate geometry (of diameter 35 mm) with a gap h = 0.5 mm. The samples were preheated in the liquid state and introduced in the rheometer thermalized at least 10 °C above the gel melting temperature. Evaporation effects could be minimized upon by using a solvent trap filled with the same solvent as that used for gelation. The sol–gel transition was achieved by cooling the sample at a rate of 2 °C min^{-1} down to a final temperature of 20 °C thanks to a Peltier module embedded in the bottom plate. The viscous (G'') and elastic (G') moduli, together with the gap distance (h) and the normal force F, were recorded as a function of time during the cooling process at a frequency f = 1 Hz and strain amplitude γ = 0.1%.

Two protocols were implemented during cooling: one at constant gap h = 0.5 mm and another one at constant normal force F = 0 N. The procedure involving a constant force proved to be best suited to the investigated samples. Indeed, application of a constant gap protocol was found to produce large drops in the viscoelastic moduli, most likely due to syneresis phenomena associated with partial detachment of the gel samples from the upper plate (see drop observed at around t = 700 s in Fig. S5A, ESI†). This problem could be avoided by using the zero normal force protocol (Fig. S5b, ESI†).[46,47]

Further rheological measurements were carried out on gels formed *in situ* and stabilized at T = 20 °C. The protocol includes frequency sweep experiments in the range f = 20 to 0.06 Hz at a strain amplitude γ = 0.05% to determine the linear viscoelastic spectrum of the sample, and a strain sweep experiments with a strain amplitude varying from γ = 0.01 to 500% at f = 1 Hz to characterize the gel non-linear response.

Bright field microscopy. Microscopy measurements were conducted on a Nikon Ti-eclipse inverted light microscope operating in a bright field mode. A camera (Zyla from Andor) equipped with a 10× objective was used to image the samples. The sample temperature was controlled with a dedicated Peltier cell (MHCS120i from Microptik). Samples were loaded in the liquid state in a homemade optical cell composed of a microscope slide and a cover slip separated by a 200 μm thick double-sided adhesive spacer ensuring airtightness (Gene Frame from Thermo Scientific). The sol–gel transition was achieved by

applying a cooling ramp from $T = 90$ °C to $T = 20$ °C at a rate of 0.6 °C s^{-1}.

Small angle X-ray scattering. The structural properties of the gel samples were investigated using small-angle X-ray scattering measurements carried out on the ID02 beamline at the European Synchrotron Radiation Facility (ESRF, Grenoble, France)[48] where an incident X-ray beam of wavelength 0.1 nm was collimated to a vertical size of 50 μm and an horizontal size of 100 μm. The sample in the liquid state was introduced in a borosilicate capillary tube of diameter 2 mm and left to cool down to $T = 20$ °C. SAXS measurements were conducted on the gel state at $T = 20$ °C. The two-dimensional scattering patterns were collected using an Eiger2 4M pixel array detector. The following data reduction procedure is described elsewhere.[49] The 2D scattering pattern is isotropic. We therefore carried out an azimuthal averaging of the 2D scattering pattern and worked on the one-dimensional spectrum $I(q)$ where q is defined as the modulus of scattering vector. Background subtraction was done after the azimuthal averaging.

Atomic force microscopy. The gel structure was investigated *in situ* using atomic force microscopy. About 1.5 mL of hot solution was poured in a small Petri dish and cooled down at room temperature. Once gelation was complete, the sample was covered with pentanol for imaging in liquid. Images were acquired with a JPK Nanowizard 4 microscope (Bruker). The tip had a nominal radius of 10 nm and was mounted on a cantilever (cantilever A, All-In-One-AI, Budget Sensors) with a rigidity of 0.2 N m^{-1}.

Electrochemical impedance spectroscopy. Impedance measurements were carried out with a Biologic-ESP 300 potentiostat equipped with a built-in computer-controlled Frequency Response Analyser (FRA) operating over a frequency range of 10 mHz up to 7 MHz. A home-made one-compartment, two-electrode cell allowing us to position two identical cofacially oriented platinum electrodes at a tunable distance d has been used to estimate the conductivity of each sample. All measurements were conducted with a sample thickness $d = 5$ mm. Gel samples were formed *in situ* by injecting a hot LMWG solution into the cell. Electrical impedance measurements have been performed in a potentiostatic regime at the open circuit potential (E_{ocp}) between 10 mHz and 1 MHz using a maximum voltage of 0.01 V. Fitting the experimental Nyquist impedance diagrams, $-\mathrm{Im}(Z)$ *vs.* $\mathrm{Re}(Z)$, where Z is the sample impedance, was achieved with Z-fit (Biologic) using equivalent electrical circuits. The conductivity of the gel samples was determined after calibration of the cell using commercial KCl solutions (Fig. S10, ESI†). A 5% uncertainty range applies to the reported conductivity values (see ESI† for further details).

Cyclic voltammetry. Cyclic voltammetry measurements have been carried out with an ESP-300 Biologic potentiostat equipped with a 1 A/48 V booster and an analogic linear scan generator. All experiments have been conducted under an argon atmosphere (glove box under N_2) in a 1 mm optical path spectroelectrochemistry quartz cuvette/cell. Lithium bis(trifluoromethylsulfonyl)imide (10^{-1} M) and tetra-*n*-butylammonium iodide (5×10^{-2} M) were used together as supporting electrolyte in 1-pentanol. 1-Pentanol was dried over alumina before use. An automatic ohmic drop compensation procedure was systematically implemented prior to recording CV data. An $Ag/AgNO_3$ (10^{-2} M) + tetra-*n*-butylammonium perchlorate (10^{-1} M) in CH_3CN electrode was used as a reference (ALS Co. Ltd). Measurements have been conducted at 20 °C using a platinum grid working electrode and a cylinder/coil-shaped platinum wire as a counter-electrode isolated from the electrolytic solution through an ionic bridge.

Results and discussion

Formulation of the conductive gel

Synthesis of the gelator. The two-step synthesis of $\mathbf{1}(Br)_2$ is summarized in Scheme 1. The latter was synthesized by modifying a procedure described by Lu and collaborators.[45] The main problem encountered when using the reported procedure was the co-precipitation of the mono-alkylated intermediate, which could hardly be removed from the isolated samples. This problem was eventually circumvented by performing the synthesis in dimethylformamide (DMF), which proved to be polar enough to solubilize the mono-alkylated intermediate. The key precursor **2** was obtained in 60% yield as the product of a Steglich esterification between 6-bromohexanoic acid and cholesterol (**3** in Scheme 1). Heating up a mixture of **2** and 4,4′-bipyridine in DMF for more than four days led to the precipitation of the targeted LMWG $\mathbf{1}(Br)_2$, which could be isolated in 53% yield by simple filtration. The latter was found to be sparingly soluble at room temperature in most common solvents and could only be dissolved after heating in polar solvents like dimethylsulfoxide (DMSO) or alcohols.

Screening of gelation conditions. Gelation was observed when cooling down hot solutions of $\mathbf{1}(Br)_2$ ($\leq$ 1% in weight) in 1-butanol, 1-pentanol, 1-hexanol, 1-heptanol, and in mixtures of 1-hexanol and 1-octanol (up to 50% volume of octanol). The temperature required to reach full solubilization of $\mathbf{1}(Br)_2$ ranged from 80 to 110 °C depending on the experimental conditions (solvent, additives). The formation of gels was first established on the ground of simple inversion tests (Table 1). Gels formed in hexanol, heptanol, and hexanol/octanol were found to be less transparent and more fragile than those obtained in butanol and pentanol (for a similar concentration in $\mathbf{1}(Br)_2$). We therefore focused our attention on these two particular solvents. Further studies revealed that the minimum gelation concentration (mgc) is around 0.1 wt% (0.6 mM) in both solvents to give weak but highly transparent gels (Fig. 1A). For concentrations above 0.4 wt%, only heterogeneous gels could be obtained due to the precipitation of $\mathbf{1}(Br)_2$ during the cooling step.

Further studies revealed that the maximum solubility of $\mathbf{1}(Br)_2$ in pure pentanol or butanol is only around 0.4 wt% at the boiling point of the solvents, which prevented us from accessing more concentrated gels. This limitation led us to explore different strategies to improve the solubility of $\mathbf{1}^{2+}$ through anion exchange. In doing so, we discovered that the

Table 1 Screening of gelation conditions

Solvent	Gelator concentration (wt%)	LiTFSI (nb. of eq.)	$T_{Solubilization}$ (°C)	Inverted vial test[a]	Transparent	Resistance to shearing[a]
Butanol	0.1–0.3	0	80–110	Yes	Yes	No
Butanol	0.4–1	0	>110	Yes	No	No
Butanol	0.1–0.3	1	80–100	Yes	Yes	No
Butanol	0.4–1	1	80–110	Yes	Yes	Yes
Pentanol	0.4–1	1	80–110	Yes	Yes	Yes
Hexanol	0.4	2	100	Yes	Yes	No
Heptanol	0.8	4	95	Yes	No	No
Octanol	0.8	2	95	No	—	—
Hexanol/Octanol 1 : 1	0.6	2	95	Yes	Yes	No

[a] See details in part 2.2 of the experimental section.

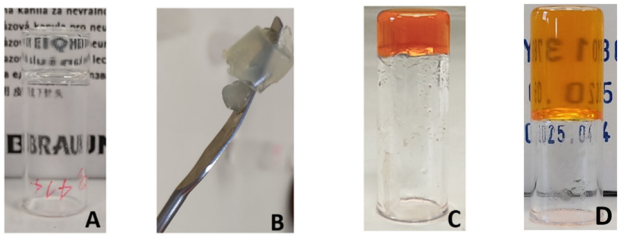

Fig. 1 Photos of gels obtained in different gelation conditions, adding or not lithium bis(trifluoromethanesulfonyle) (LiTFSI) or tetrabuthylammonium iodide (TBAI) in the gel composition. (A) [**1**$(Br)_2$] = 0.6 mM (0.1 wt%) in BuOH. (B) [**1**$(Br)_2$] = 2.5 mM (0.4 wt%), [LiTFSI] = 2.5 mM. (C) [**1**$(Br)_2$] = 2.5 mM, [TBAI] = 0.1 M in BuOH. (D) [**1**$(Br)_2$] = 1.3 mM (0.2 wt%), [LiTFSI] = 100 mM, [TBAI] = 50 mM in Pentanol. Vial diameter is *ca.* 1 cm.

maximum solubility could be significantly enhanced, up to 1 wt%, by the addition of lithium bis(trifluoromethansulfonyl)-imide (LiTFSI). This additive allowed us to increase the gelator concentration and to produce much stiffer gels which proved to be transparent, demoldable and ''healable'', as revealed by their ability to reform after being mixed/sheared with a spatula (Fig. 1B). Addition of more than four molar equivalents of LiTFSI was nevertheless found to be detrimental to the self-assembly of $\mathbf{1}^{2+}$, as revealed by the formation of weaker gels or by the absence of gelation. This was confirmed by studying the properties of gels formed with **1**$(TFSI)_2$, obtained as the product of an ion metathesis reaction between **1**$(Br)_2$ and LiTFSI (see ESI† section for details and Fig. 1C and D). Replacement of the bromine by TFSI anions was found to result in a tenfold increase of the mgc and in the systematic formation of opaque heterogeneous gels. These findings thus support the conclusion that TFSI anions improve the solubility of $\mathbf{1}^{2+}$ but impair its self-assembly. Experimentally, we found that the most homogeneous and transparent gels could be obtained when using LiTFSI as an additive with a LiTFSI: **1**$(Br)_2$ ratio kept between **1** and **3**.

Further investigations revealed that the ionic strength of the gels could also be significantly increased without impacting their bulk properties. Gels could indeed be obtained in the presence of large quantities of ionic additives such as tetra-*n*-butylammonium iodide (TBAI) and lithium bis(trifluoromethanesulfonyl)imide (LiTFSI) in butanol and pentanol (up to molar concentrations) without affecting their homogeneity and transparency. Gels formed in such conditions were found to exhibit an intense orange coloration attributed to the formation of charge transfer (CT) complexes between the viologen acceptors and the iodide donors.

Optimisation of the ionic content. The relative influence of the different anions used in our experimental procedures, namely Br^-, I^- and $TFSI^-$, on gelation was first assessed by studying the change in the gel–sol transition temperature (T_g) value as a function of the $[TFSI^-]/[Br^-]$ and $[TFSI^-]/[I^-]$ ratio (Fig. 2). This study aimed both at confirming quantitatively the trends observed during the screening phase (effect of $TFSI^-$ ions) (Fig. 2A) and at characterizing the properties of gels containing large amounts of ions (Fig. 2B). T_g was determined for each mixture from temperature sweep rheological measurements (see ESI† for details). A significant decrease in T_g was observed when adding increasing amounts of LiTFSI to hot solutions of **1**$(Br)_2$ (0.2 wt%, 1.3 mM in **1**$(Br)_2$). The data shown in Fig. 2A reveal that the addition of $TFSI^-$ decreases the

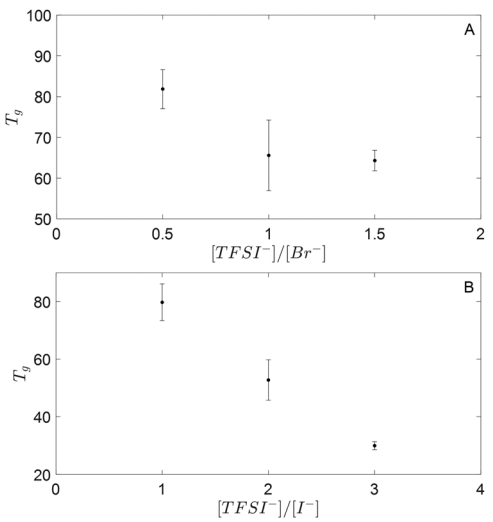

Fig. 2 Influence of the concentration ratio between bistrifluoromethysulfionylimide ($TFSI^-$) and halide ions on the gelation temperature (T_g) in pentanol. Each point corresponds to the mean value obtained for a series of rheological measurements, the error bar corresponds to the standard deviation of the series. (A) For all samples tested [**1**$(Br)_2$] = 0.2 wt% = 1.3 mM in pentanol, the source of $TFSI^-$ anions was LiTFSI. (B) For all samples tested [$TFSI^-$] = 100 mM, [**1**$(Br)_2$] = 0.2 wt% = 1.3 mM in pentanol, the source of I^- anions is TBAI.

gelation temperature from 80 °C to 65 °C. It is also worth mentioning that the addition of LiTFSI in excess ($[TFSI^-]/[Br^-] \geq 2.5$) resulted in the formation of heterogeneous gels made of large aggregates.

The data plotted in Fig. 2B were collected for gel samples featuring fixed concentrations in LiTFSI (100 mM) and $\mathbf{1}(Br)_2$ (0.2 wt% = 1.3 mM) and different concentrations in TBAI. Those data bring to light the utmost impact of the $[TFSI^-]/[I^-]$ ratio on the gelation temperature, which is found to decrease from 80 °C to 30 °C as the $[TFSI^-]/[I^-]$ ratio increases from 1 to 3. These measurements also revealed that this large drop in T_g occurs while other key rheological characteristics of the gel, such as the elastic modulus remain constant. This study also revealed that a decrease in the concentration in iodide down to $[TFSI^-]/[I^-] = 4$ leads to the formation of heterogeneous materials (Fig. S14, ESI†).

Altogether, these results are consistent with the conclusion that both the solubility and the gelation temperature of $\mathbf{1}^{2+}$ are significantly improved when replacing the halides counteranions by $TFSI^-$ and that the most relevant parameters to best analyze/understand the gelation process are the concentration ratios $[TFSI^-]/[Br^-]$ or $[TFSI^-]/[I^-]$. Futhermore, this screening also revealed that both LiTFSI and TBAI are needed to form robust and transparent gels.

Further studies aimed at investigating the effect of these additives (TBAI and LiTFSI) on the ionic conductivity of the gels (Fig. 3 and Table S2, ESI†). These measurements were conducted on samples featuring a fixed $[TFSI^-]/[I^-]$ ratio and concentration in $\mathbf{1}^{2+}$ (0.2 wt%) so as to ensure the formation of robust and homogeneous gels with moderate T_g values. The amount of added salts was found to be limited by their respective solubilities in pentanol, *i.e.* 100 mM for LiTFSI and 50 mM for TBAI. The electrolyte resistance (R_e) and the associated ionic conductivities (σ) were determined for each sample by fitting the experimental Nyquist impedance diagrams (Im(Z) *vs.* Re(Z)) collected in a home-made cell with a Randles-like electrical circuits (see ESI† for details).

The data plotted in Fig. 3 reveal that the conductivity of the gels increases linearly with the total concentration in ions and that the measured values are equivalent to those measured for reference pentanol solutions exhibiting the same ionic composition. The addition of TBAI and LiTFSI made it possible to achieve fairly high conductivity values, reaching 530 μS cm^{-1} for a composition of 100 mM in LiTFSI and 50 mM in TBAI. The effect of added ions is also clearly put forward when comparing the conductivity values discussed above with that of 3 μS cm^{-1} measured for a gel obtained from [1(Br)2] in BuOH(0.4 wt%). Interestingly, we found that using TBAI and LiTFSI at concentrations exceeding their solubility in pentanol (total concentration >150 mM) led to the formation of a homogeneous gel, reaching a conductivity of 900 μS cm^{-1}. It should be mentioned that these values lie within the range of ionic conductivity previously observed for ionogels and supramolecular electrolytes.[19,22]

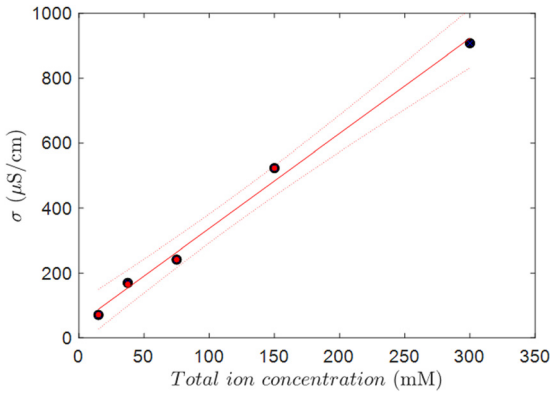

Fig. 3 Evolution of the ionic conductivity with the total concentration in salts ($[TFSI^-]/[I^-]$ = 2 in all experiments). Black dots represent the ionic conductivity measured for gels obtained from the self-assembly of $\mathbf{1}(Br)_2$ (0.2 wt% in pentanol). Red dots correspond to the ionic conductivity measured for reference solutions of TBAI + LiTFSI salts in pentanol. The continuous red line and dotted lines correspond to the best linear fit and to the corresponding confidence boundary, respectively.

Structural characterization

UV-Vis spectroscopy. The sol–gel transition has been first characterized by UV-vis absorption measurements. The spectra recorded over time (1 spectrum/s over a total duration of 10 min) during the cooling/gelation of a hot solution ($[\mathbf{1}(Br)_2]$ = 1.3 mM, [LiTFSI] = 100 mM, [TBAI] = 50 mM in pentanol) are shown in Fig. 4. These data reveal that the sol–gel transition observed upon cooling results in the development of a broad absorption band centered at λ_{max} = 440 nm, attributed to charge transfer (CT)[50] from the iodide donors to the viologen acceptors. In support of the proposed attribution, we found that the bright orange color of the gel is observed only in the presence of iodide and not with bromides, and that the intensity of the $\{I^-.\mathbf{1}^{2+}\}$ CT band increases with the concentration in gelator (see Fig. S12, ESI†) or with the $[I^-]/[TFSI^-]$ ratio (see Fig. S14, ESI†).

Consistent with their weaker donating character, replacing iodides with bromides led to the formation of colorless

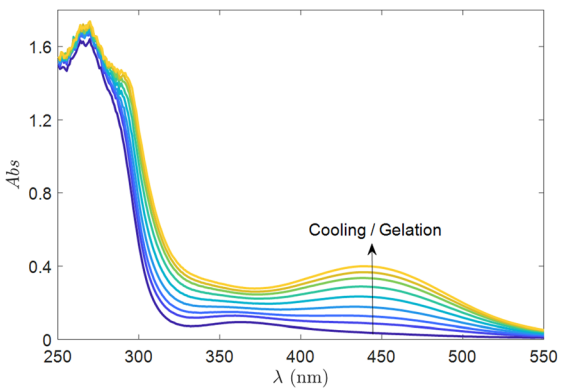

Fig. 4 UV-vis absorbance spectra recorded over time during slow cooling of a hot solution of $\mathbf{1}(Br)_2$/LiTFSI/TBAI in pentanol ($[\mathbf{1}(Br)_2]$ = 1.3 mM, [LiTFSI] = 100 mM, [TBAI] = 50 mM) down to room temperature. Gelation of the sample upon cooling results in the development of a broad band at λ_{max} = 440 nm.

transparent gels featuring a blue-shifted CT band at λ_{max} = 350 nm (Fig. S13, ESI†), while the addition of chlorides resulted in the precipitation of $\mathbf{1}(Cl)_2$. Additional studies also revealed that the intensity of these CT bands observed in the gel state gradually decreases upon the addition of increasing amounts of $TFSI^-$ anions (Fig. S13 and S14, ESI†) but that too much $TFSI^-$ prevents gelation, which indicates that part of the halides in the gel can be exchanged by $TFSI^-$ but that their presence is required to ensure gelation. Moreover, the fact that the CT bands at 350 nm $\{Br^-.\mathbf{1}^{2+}\}$ or 440 nm $\{I^-.\mathbf{1}^{2+}\}$ disappear when converting gels into solutions by heating, and that they reappear with the back-gelation triggered by cooling led us to conclude that these CT complexes formed with halides play a major role in the self-assembly process leading to gelation.[51]

Electronic circular dichroism. The gelation of $\mathbf{1}^{2+}$ was found to involve the formation of chiral assemblies. This unexpected feature initially uncovered by Lu and coworkers,[45] can be revealed by electronic circular dichroism (ECD) measurements through the observation of intense signatures developing during gelation. The ECD spectra collected over time during cooling/gelation of a hot solution of $\mathbf{1}(Br)_2$ containing TBAI and LiTFSI are shown in Fig. 5A.

These data reveal that the initial hot solution is ECD-silent and that the intense ECD band at λ_{max} = 273 nm only develops upon gelation. Further studies showed that the intensity of this viologen-centered ECD band eventually disappears upon heating the gel sample above the T_g value, *i.e.*, upon the gel–sol transition, and can be fully restored by cooling the solution until gelation is observed again. This fully reversible process thus supports the conclusion that the ECD signal results from the long-range organization of the dicationic viologen units into chiral assemblies. The broad band of lower intensity observed from 350 to 550 nm on the CD spectra (Fig. 5A), is even more visible on the curve representing the absorption dissymmetry factor (g_{abs} = ΔAbs/Abs) as a function of the wavelength (Fig. 5B). This band, attributed to the formation of $\{I^-.\mathbf{1}^{2+}\}$ CT complexes, demonstrates the key role of the I^- anions in the self-assembly leading to chiral gels (a similar behavior observed with $\{Br^-.\mathbf{1}^{2+}\}$ is shown in Fig. S13C, ESI†). The contribution of these CT complexes to the ECD spectra thus supports the conclusion that the I^- (or Br^-) anions are structuring elements of the chiral assembly.

These data thus led us to propose that chirality results from the formation of helicoidal stacks between positively charged viologens and negatively charged halides, with a helicity imposed by the torsion angle between each successive viologen unit in the stack. Theoretical calculations using coarse-grained models to simulate the assembly are currently underway to confirm this hypothesis. The resulting assembly is held together by a combination of attractive supramolecular interactions, including electrostatic forces and donor–acceptor interactions, which can be weakened and eventually broken by the replacement of the halides by TFSI anions, as demonstrated by a decrease in the T_g values (Fig. 2) and by the observation of much weaker CT absorbance band (Fig. S13 and S14, ESI†) and CD signals (Fig. S15, ESI†).

Microscopy, AFM and SAXS. The gel structure was also determined using a combination of bright-field microscopy, AFM, and SAXS measurements. One key conclusion drawn from the data shown in Fig. 6 is that the investigated gels display a very well-defined hierarchical structure. At the macroscopic level, microscope images recorded over time for a hot dispersion subjected to cooling from 90 °C to 20 °C at a rate of 0.6 °C s^{-1} (Fig. 6A) revealed the nucleation and growth spheroidal domains with dendrit-like internal structure at the micrometer scale (Fig. 6A).[52,53] As the temperature is decreased, the size of these spheroidal domains increases up to the point where they interpenetrate, thus forming a percolating network. Such a percolation most likely corresponds to the point where the sample becomes a gel. The typical size ξ of the spheroids at that point is estimated to be 200 μm.

At length scales ranging between 10 nm and a few micrometers, AFM images revealed that the spheroidal domains comprise bundles of intertwined fibers (Fig. 6B). The length of these fibers can reach several micrometers, while their diameter is about 10 nm, close to the resolution limit of the present AFM images.

The small-scale structure of the fibers was further characterized by SAXS measurements. The data shown in Fig. 6C displays the scattered intensity I as a function of the modulus of scattering vector q. For the larger q values, *i.e.*, at the smaller length scales, the scattering spectrum $I(q)$ is well modelled by the spectrum of a hollow core–shell cylinder.[54] Such a spectrum is characterized by wide oscillation at large $q \sim 0.6$ nm^{-1}, and was already invoked to model the self-assembly of other

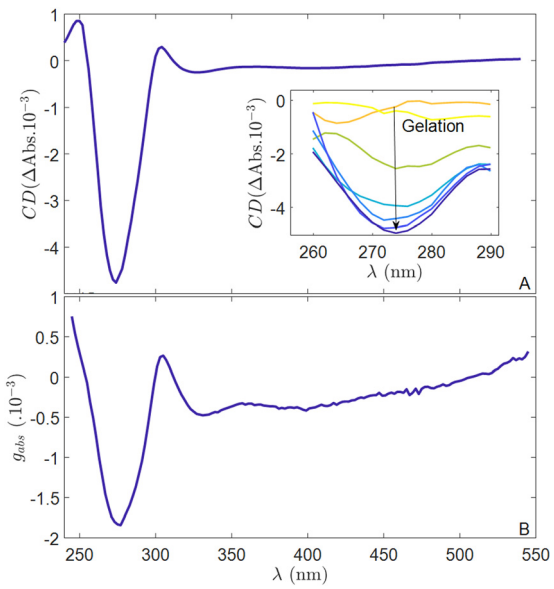

Fig. 5 (A) Electronic circular dichroism spectra collected for gels of $\mathbf{1}^{2+}$ obtained in pentanol ([$\mathbf{1}(Br)_2$] = 1.3 mM, [TBAI] = 50 mM, [LiTFSI] = 100 mM). The inset shows the evolution of the CD signal after heating the gel above T_g and the leaving it cooling down to room temperature. (B) g_{abs} spectra collected for gels of $\mathbf{1}^{2+}$ obtained in pentanol ([$\mathbf{1}(Br)_2$] = 1.3 mM, [TBAI] = 50 mM, [LiTFSI] = 100 mM). The CD and g_{abs} data collected after reaching room temperature are shown in blue color.

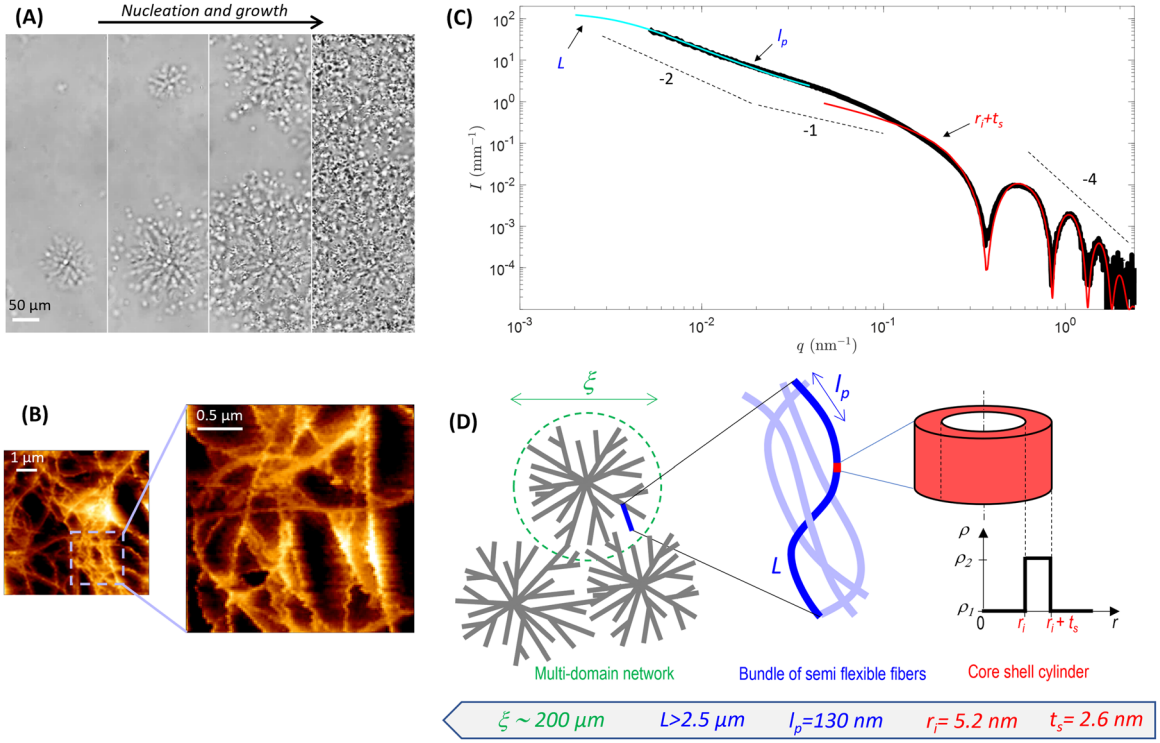

Fig. 6 Determination of the gel structure using light microscopy, AFM and SAXS ([**1**(Br)$_2$] = 1.3 mM, [TBAI] = 50 mM, [LiTFSI] = 100 mM in pentanol). (a) Microscopy bright field images of the sol–gel transition using a 15× magnification. The sol–gel transition proceeds through a nucleation and growth mechanism. (b) AFM images of the gel final state. (c) Scattering intensity $I(q)$ of the gel final state as a function of the wave vector (black line) measured using SAXS. At low q, the blue line is the best fit of $I(q)$ using an isotropic dispersion of flexible cylinders of persistence length l_p and length L (fitting range: 0.005 nm^{-1} < q < 0.04 nm^{-1}). We obtain l_p = 130 nm and L = 2.5 µm. Due to the limited range at low q, L = 2.5 µm is the smallest filament length for which the fit works. The filaments have therefore a length, L > 2.5 µm. At large q, the red line is the best fit of $I(q)$ using an isotropic dispersion of hollow core–shell cylinders of inner radius r_i = 5.2 nm and shell thickness t_s = 2.6 nm with a scattering length density difference between the solvent and the cylinder shell of $\rho_2-\rho_1$ = 0.5 10^{-6} Å^{-2} (fitting range: 0.2 nm^{-1} < q < 2 nm^{-1}) (C) Schematic of the hierarchical assembly of the gel based on the interpretation of the microscopy, the AFM, and the SAXS data.

supramolecular gels.[55] Here, as shown by the red fit in Fig. 6C (see ESI† for details on the model and fitting procedure), a hollow cylinder with inner radius r_i = 5.2 nm and shell thickness t_s = 2.6 nm, giving a total diameter of 7.8 nm, provides an excellent fit of the experimental data for q > 0.1 nm^{-1}. Note that such dimensions are consistent with the AFM images of Fig. 6B. At this stage, however, it is not clear whether the apparent helicoidal geometry of some fibers in Fig. 6B is due to artifacts in AFM images or whether such a twist is real and could result from the chirality of the building blocks. Upon decreasing q below 0.1 nm^{-1}, *i.e.*, for length scales than about 60 nm, we observe qualitatively a transition from a regime where $I \propto q^{-1}$, typical of rigid cylinders, to a regime characterized by $I \propto q^{-2}$, typical of flexible, Gaussian polymers.

More precisely, as shown by the blue fit in Fig. 6C, this transition is well captured by a flexible cylinder model[56] with persistence length of l_p = 130 nm. The contour length L of the flexible cylinder is greater than 2.5 µm, and thus falls out of the range of scales accessible to the present SAXS measurements. Consistently with AFM images, the most probable interpretation of such a modeling is that, at length scales larger than about 130 nm and up to at least 2.5 µm, the fibers are intertwined into a fractal network with fractal dimension $d_f \sim 2$. As already pointed out above, at even larger scales, the microstructure is organized into percolated spheroid domains of size ξ ~ 200 µm. The overall hierarchical assembly of the gel is sketched in Fig. 6D.

Properties of the gel

Rheological properties. The viscoelastic properties of the gels have been characterized using rheometry. The data collected using normal force-controlled rheometry for a 0.2 wt% viologen gel containing LiTFSI and TBAI ([LiTFSI] = 100 mM, [TBAI] = 50 mM in pentanol) are shown in Fig. 7. The gel was formed *in situ* from a hot solution of the gelator submitted to a 2 °C min^{-1} cooling ramp while imposing a constant normal force F = 0 N (Fig. 7A). Initially, the viscous modulus G'' is larger than the elastic modulus G' attesting that the sample is liquid. Progressive gelation of the sample is then easily revealed by the growth of G' that becomes larger than G'' after t = 1500 s. The gelation temperature was estimated from the crossover of G' and G'', which occurred at T_g = 44 °C for this particular gel. Other gels were investigated in the same way, leading to the T_g data shown in Fig. 2 (see also Table S1 in the ESI†). The curves displayed in Fig. 7A also reveal that the viscoelastic properties of the gel become stationary after 1800 s to reach, reaching

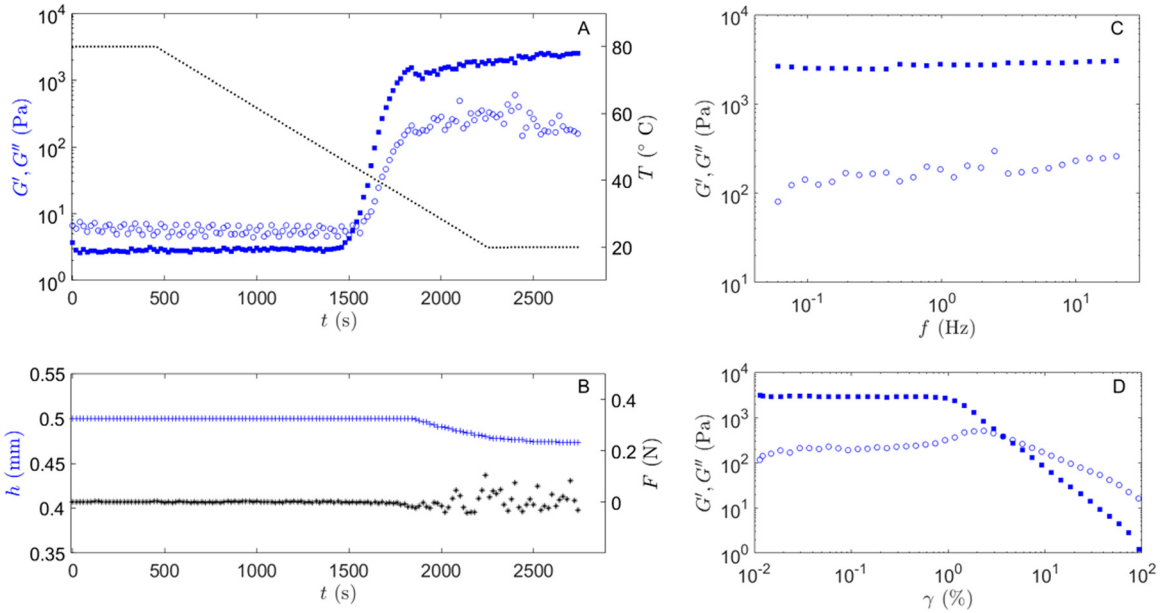

Fig. 7 Rheological characterization of a gel sample ([**1**(Br)$_2$] = 1.3 mM, [LiTFSI] = 100 mM, [TBAI] = 50 mM in pentanol). (A) Evolution of the viscous (hollow circles) and elastic (full blue squares) moduli in semilogarithmic scales determined through small-amplitude oscillations with γ = 0.1% and f = 1 Hz during a cooling ramp of 2 °C min^{-1} (T in black dots), (crossover temperature of G' and G'': T_g = 44 °C determined at the crossing of the blue curves for t = 1540 s; terminal value of the elastic modulus: G' = 1700–2200 Pa; terminal value of the viscous modulus: G'' = 150–300 Pa). (B) Evolution of the gap width h (blue crosses) while imposing a constant normal force F (black stars) during the cooling ramp (relative decrease of the gap width: $\Delta h/h$ = 4.8%. (C) Frequency sweep experiment conducted between 20 Hz and 0.06 Hz on the freshly *in situ* formed gel, 10 pts/decade, γ = 0.05%. (D) Strain sweep experiment conducted for γ = 0.01% up to 500% on the freshly *in situ* formed gel (yield strain value: γ_y = 4%).

G' = 2000 Pa and G'' = 150–300 Pa at T = 20 °C. It should be mentioned that these changes in the rheological properties of the sample were found to be accompanied by a significant contraction of the sample, which could be estimated from the decrease in the gap width ($\Delta h/h$ = 4.8%, see Fig. 7B).

The viscoelastic spectrum presented in Fig. 7C also reveals that the G' and G'' values are almost frequency independent over the investigated frequency range and that the elastic modulus remains much larger than viscous modulus (G' = 2500 Pa, G'' = 150 Pa). Fig. 7D displays the non-linear mechanical properties of the gel investigated through a strain sweep experiment, where we measured the evolution of the viscoelastic moduli as the amplitude of the oscillatory strain γ is ramped up. At small amplitudes, up to γ = 0.7%, the material is probed in the linear viscoelastic regime. Beyond γ = 0.7%, G' weakens and G'' increases indicating plastic rearrangements, which eventually leads to rupture at the yield strain γ_y = 4% defined as the strain for which G' = G''. Above γ_y, the gel flows and G'' > G'. The gel thus shows viscoelastic properties typical of soft solids: a viscoelastic sprectrum that is frequency independent and that gives way to liquid-like behavior above a yield strain γ_y = 4%.

Conductive properties. Mixing **1**(Br)$_2$, TBAI, and LiTFSI in pentanol allowed us to form robust and transparent gels containing high concentrations of mobile ionic species (Fig. 1D). The ionic conductivity of those gels was determined through AC-impedance spectroscopy measurements. The Nyquist plot, showing the imaginary part *vs.* the real part of the impedance (Z), recorded at 25 °C in a home-made thermostated cell, is represented in Fig. 8A. The latter exhibits a semicircle at high frequencies followed by a linear increase at lower frequencies attributed to the Warburg impedance arising from the semi-infinite diffusion of ions at the electrode.[57] This type of Nyquist plots is usually found for systems switching from charge transfer control at high

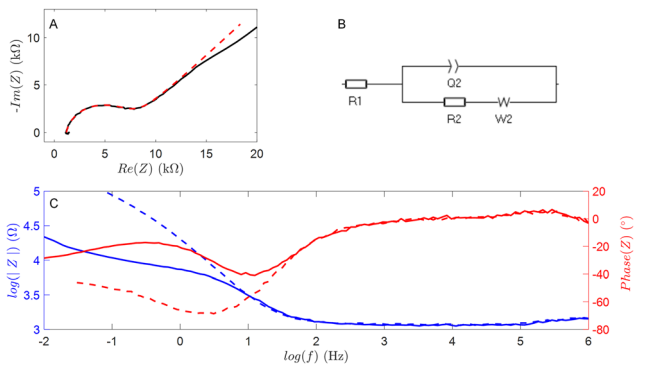

Fig. 8 (A) Black line: Nyquist plot of a gel sample ([**1**(Br)$_2$] = 1.3 mM (0.2 wt%), [LiTFSI] = 100 mM, [TBAI] = 50 mM in pentanol). Red dashed lines: Nyquist plot corresponding to the equivalent circuit used to fit experimental data. (B) Equivalent circuit used to fit experimental data ($R1$ = 1 190 Ω, $Q2$ = 8.804 μFs$^{-0.104}$, $R2$ = 6 074 Ω, $W2$ = 2657 (1–j)/(2πf)$^{0.5}$. (C) Full lines: Bode plot of a gel sample ([**1**(Br)$_2$] = 1.3 mM (0.2 wt%), [LiTFSI] = 100 mM, [TBAI] = 50 mM in pentanol). Dashed lines: Bode plot collected for a solution of LiTFSI and TBAI in pentanol ([LiTFSI] = 100 mM, [TBAI] = 50 mM). The impedance modulus is shown in blue and the impedance phase in red.

frequencies to diffusion control at low frequencies.[58] The frequency response could then be fitted with an equivalent circuit containing two resistances ($R1$, $R2$), one Warburg impedance ($W2$), and a constant phase element ($Q2$) connected in parallel to $R2$ and $W2$ (Fig. 8A).

The Bode plots (showing the frequency dependence of the impedance modulus and phase) recorded for a gel sample and for a reference solution of only TBAI and LiTFSI in pentanol are compared in Fig. 8A. Both samples exhibit a high-frequency resistive plateau at $\phi = 0^\circ$ (phase angle, red curves) and $|Z| = 1120\ \Omega$ (impedance, blue curve), which allows us to estimate the resistance ($R1$) associated with the migration of ionic species in the gel. The fact that this plateau perfectly fits the ionic resistance values calculated for the gelator-free electrolyte solutions (Fig. 8C) can be explained by the relatively low concentration in gelator ($< 1\%$ wt) and by the porosity of the network in the gel samples. As described in the literature for ionogels containing low concentrations in gelators, the pores of the fibrillar network are, in most cases, large enough not to hinder the diffusion of ionic species, resulting in gels as conductive as the liquid gelator-free electrolyte.[19]

Major differences between both samples are conversely observed in the low-frequency domain. Below 50 Hz, the impedance of the saline solution is seen to increase gradually due to the polarization of the constant phase element, while the curve collected with the gel sample shows a plateau from 5 to 0.1 Hz. This plateau coincides with a local phase minimum corresponding to a quasi-resistive behaviour for which the impedance value is roughly $R1 + R2$. Observation of such a plateau at low frequency is thus consistent with the existence of a charge transfer resistance ($R2$) corresponding to electron transfers from the electrode to the viologen moiety. This value of $R2 = 6000\ \Omega$ was also confirmed by electrochemical measurements (see Fig. S11, ESI†) from the slope of the $i = f(\eta)$ curves at $\eta \sim 0$ V.

Taken together, these impedance data (Fig. 3 and Fig. 8) thus reveal that the investigated gels are very efficient ionic conductors, as good as reference electrolyte solutions. They also suggest that the presence of redox-active viologen units provides the gels with electron-conducting capabilities. Additional studies are currently under way to further support this conclusion.

These conductive gels have also been characterized by electrochemical methods. Cyclic voltammetry measurements were carried out in a home-made three electrodes cell on gels formed *in situ* after cooling a mixture of $\mathbf{1}(Br)_2$, TBAI and LiTFSI in pentanol. The CV curve recorded at a platinum grid working electrode (Fig. 9) shows two reduction waves at $[E_{1/2}]^1 = -0.61$ V and $[E_{1/2}]^2 = -1.04$ V attributed to the successive formation of the viologen-based cation radical $1^{+\bullet}$ and of the neutral quinonic species 1^0. Observation of two one-electron reduction waves is thus consistent with the EIS data discussed above, revealing that an ''injection of charges'' can be involved with gels samples incorporating the redox-active species $\mathbf{1}^{2+}$. The diffusion-controlled shape and weak intensity of the signals observed in Fig. 9 also support the conclusion that the measured faradaic current results from the reduction of ''free'' viologen units present in solution in equilibrium with the micrometric dendritic clusters seen in Fig. 6.

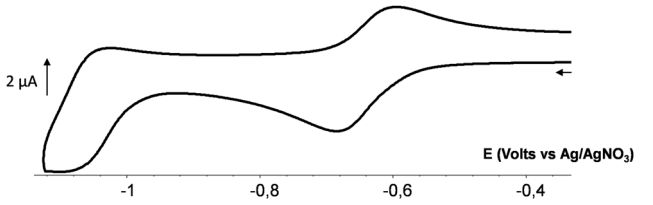

Fig. 9 Cyclic voltammogram of the $\mathbf{1}^{2+}$ gel in 1-pentanol ([TBAI] = 50 mM, [LiTFSI] = 100 mM, [$\mathbf{1}(Br)_2$] = 1.3 mM). Fresh gel formed around a Pt grid used as working electrode, $v = 10$ mV s^{-1}.

It should be mentioned here that there are very few examples of electroactive supramolecular gels described in the literature and that the rare cases described to date only concern organic/inorganic hybrid systems based on viologen/carbon nanotubes[44] or peptides/heteropoly acids[44,59] self-assembly. The conductive gels described in the present articles are thus promising candidates for the development of electron-responsive soft materials both in terms of electrochemical addressability and reversibility. Further investigations are currently underway to characterize their electron/photo-responsiveness.

Conclusions

We have reported detailed structural, rheological, and electrical characterizations of supramolecular gels obtained by self-assembly of a dicationic low molecular weight gelator incorporating a cholesterol-substituted 4,4′-bipyridinium. This molecule has been shown to self-assemble in pentanol to form chiral hollow core–shell cylinders of inner radius $r_i = 5.2$ nm and shell thickness $t_s = 2.6$ nm. These cylinders are very long and become flexible above $l_p = 130$ nm, curling and branching into a fractal structure. We also showed that the optical, rheological, and electrical properties of the gels can be tuned by the addition of ionic additives. The gelation process and the structure/properties of the gel have been thoroughly investigated by UV-Vis and ECD spectroscopy, rheology, bright-field microscopy, SAXS, AFM, electrochemical and Impedance measurements. Our results demonstrate that the ionic composition of the gel can be easily tuned to afford robust, transparent, conductive, and chiral gels.

Conflicts of interest

There are no conflicts to declare.

Acknowledgements

The authors thank the Ecole Normale Supérieure de Lyon (ENSL) and the Centre National de la Recherche Scientifique (CNRS) for financial, logistical, and administrative supports. The authors thank the ESRF for beamtime at the beamline ID02

and Theyencheri Narayanan for discussions and technical support for the USAXS measurements. This work was supported by the LABEX iMUST (ANR-10-LABX-0064) of Université de Lyon within the program ''Investissements d'Avenir'' (ANR-11-IDEX-0007) operated by the French National Research Agency (ANR), by the ANR ANGEL (ANR-21-CE06-0020), by the ANR ChiroSwitch (ANR-22-CE06-0012) and by the ''Mission pour les initiatives transverses et interdisciplinaires'' MITI CNRS (Auto-organisation AAP 2020). V. A. thanks ENSL for the CDSN PhD Grant.

Notes and references

1 P. Terech and R. G. Weiss, *Chem. Rev.*, 1997, **97**, 3133–3160.
2 S. S. Babu, V. K. Praveen and A. Ajayaghosh, *Chem. Rev.*, 2014, **114**, 1973–2129.
3 E. R. Draper and D. J. Adams, *Chem*, 2017, **3**, 390–410.
4 C. Echeverria, S. N. Fernandes, M. H. Godinho, J. P. Borges and P. I. P. Soares, *Gels*, 2018, **4**, 54.
5 C. D. Jones and J. W. Steed, *Chem. Soc. Rev.*, 2016, **45**, 6546–6596.
6 S. Panja and D. J. Adams, *Chem. Soc. Rev.*, 2021, **50**, 5165–5200.
7 W. Fang, Y. Zhang, J. Wu, C. Liu, H. Zhu and T. Tu, *Chem. – Eur. J.*, 2018, **13**, 712–729.
8 Y. Wang, D. Astruc and A. S. Abd-El-Aziz, *Chem. Soc. Rev.*, 2019, **48**, 558–636.
9 G. I. Dzhardimalieva, B. C. Yadav, S. Singh and I. E. Uflyand, *Dalton Trans.*, 2020, **49**, 3042–3087.
10 B. O. Okesola and D. K. Smith, *Chem. Soc. Rev.*, 2016, **45**, 4226–4251.
11 N. Falcone and H.-B. Kraatz, *Chem. – Eur. J.*, 2018, **24**, 14316–14328.
12 H. Wu, J. Zheng, A.-L. Kjøniksen, W. Wang, Y. Zhang and J. Ma, *Adv. Mater.*, 2019, **31**, 1806204.
13 M. Häring and D. D. Díaz, *Chem. Commun.*, 2016, **52**, 13068–13081.
14 J. Zhang and C.-Y. Su, *Coord. Chem. Rev.*, 2013, **257**, 1373–1408.
15 J. H. Jung, J. H. Lee, J. R. Silverman and G. John, *Chem. Soc. Rev.*, 2013, **42**, 924–936.
16 Y. Kumar, C. Mahendar, A. Kalam and M. Dubey, *Sustain. Energy Fuels*, 2021, **5**, 1708–1713.
17 Y. Kumar and M. Dubey, *Chem. Commun.*, 2022, **58**, 549–552.
18 C. Mahendar, Y. Kumar, M. K. Dixit, M. Mukherjee, A. Kalam and M. Dubey, *Mol. Syst. Des. Eng.*, 2021, **6**, 654–661.
19 W. P. Singh, U. Koch and R. S. Singh, *Soft Mater.*, 2020, **18**, 386–410.
20 S. Xu, X. Liang, K. Ge, H. Yuan and G. Liu, *ACS Appl. Energy Mater.*, 2022, **5**(3), 2929–2936.
21 J. H. Lee, A. S. Lee, J.-C. Lee, S. M. Hong, S. S. Hwang and C. M. Koo, *J. Mater. Chem. A*, 2015, **3**, 2226–2233.
22 J. Xie, B.-Q. Li, Y.-W. Song, H.-J. Peng and Q. Zhang, *Batteries Supercaps*, 2020, **3**, 47–51.
23 P. Wang, S. M. Zakeeruddin, P. Comte, I. Exnar and M. Grätzel, *J. Am. Chem. Soc.*, 2003, **125**, 1166–1167.
24 W. Zhang, Z. Wang, K. Chen, L. Li, L. Tao, J. Zhang and H. Wang, *Mater. Chem. Phys.*, 2019, **221**, 430–435.
25 A. S. Shaplov, R. Marcilla and D. Mecerreyes, *Electrochim. Acta*, 2015, **175**, 18–34.
26 T. J. Trivedi, D. Bhattacharjya, J.-S. Yu and A. Kumar, *ChemSusChem*, 2015, **8**, 3294–3303.
27 Q. Yu, Y. Wu, D. Li, M. Cai, F. Zhou and W. Liu, *J. Colloid Interface Sci.*, 2017, **487**, 130–140.
28 C. Kahlfuss, T. Gibaud, S. Denis-Quanquin, S. Chowdhury, G. Royal, F. Chevallier, E. Saint-Aman and C. Bucher, *Chem. – Eur. J.*, 2018, **24**, 13009–13019.
29 S. Chowdhury, Q. Reynard-Feytis, C. Roizard, D. Frath, F. Chevallier, C. Bucher and T. Gibaud, *J. Phys. Chem. B*, 2021, **125**, 12063–12071.
30 C. Roizard, V. Andrieux, S. Al Shehimy, S. Chowdhury, Q. Reynard-Feytis, C. Kahlfuss, E. Saint-Aman, F. Chevallier, C. Bucher, T. Gibaud and D. Frath, *ECS Adv.*, 2022, **1**, 020502.
31 N. Mercier, *Eur. J. Inorg. Chem.*, 2013, 19–31.
32 L. Striepe and T. Baumgartner, *Chem. – Eur. J.*, 2017, **23**, 16924–16940.
33 M. Kathiresan, B. Ambrose, N. Angulakshmi, D. E. Mathew, D. Sujatha and A. M. Stephan, *J. Mater. Chem. A*, 2021, **9**, 27215–27233.
34 H. Chen, V. Brasiliense, J. Mo, L. Zhang, Y. Jiao, Z. Chen, L. O. Jones, G. He, Q.-H. Guo, X.-Y. Chen, B. Song, G. C. Schatz and J. F. Stoddart, *J. Am. Chem. Soc.*, 2021, **143**, 2886–2895.
35 J. Li, S. Pudar, H. Yu, S. Li, J. S. Moore, J. Rodríguez-López, N. E. Jackson and C. M. Schroeder, *J. Phys. Chem. C*, 2021, **125**, 21862–21872.
36 Q. V. Nguyen, P. Martin, D. Frath, M. L. Della Rocca, F. Lafolet, S. Bellinck, P. Lafarge and J.-C. Lacroix, *J. Am. Chem. Soc.*, 2018, **140**, 10131–10134.
37 Y. Han, C. Nickle, Z. Zhang, H. P. A. G. Astier, T. J. Duffin, D. Qi, Z. Wang, E. del Barco, D. Thompson and C. A. Nijhuis, *Nat. Mater.*, 2020, **19**, 843–848.
38 K. V. Rao, K. Jayaramulu, T. K. Maji and S. J. George, *Angew. Chem., Int. Ed.*, 2010, **49**, 4218–4222.
39 S. Datta, N. Dey and S. Bhattacharya, *Chem. Commun.*, 2017, **53**, 2371–2374.
40 T. Yuan, M. Vazquez, A. N. Goldner, Y. Xu, R. Contrucci, M. A. Firestone, M. A. Olson and L. Fang, *Adv. Funct. Mater.*, 2016, **26**, 8604–8612.
41 S. Dhiman, K. Jalani and S. J. George, *ACS Appl. Mater. Interfaces*, 2020, **12**, 5259–5264.
42 T. Yuan, Y. Xu, C. Zhu, Z. Jiang, H.-J. Sue, L. Fang and M. A. Olson, *Chem. Mater.*, 2017, **29**, 9937–9945.
43 M. Suzuki, C. C. Waraksa, H. Nakayama, K. Hanabusa, M. Kimura and H. Shirai, *Chem. Commun.*, 2001, 2012–2013.
44 S. Datta and S. Bhattacharya, *Chem. – Eur. J.*, 2016, **22**, 7524–7532.
45 P. Xue, R. Lu, D. Li, M. Jin, C. Bao, Y. Zhao and Z. Wang, *Chem. Mater.*, 2004, **16**, 3702–3707.
46 B. Mao, T. Divoux and P. Snabre, *J. Rheol.*, 2016, **60**, 473–489.

47 R. Beniazza, N. Bayo, D. Jardel, R. Rust, B. Mao, T. Divoux, M. Schmutz, F. Castet, G. Raffy, A. Del Guerzo, N. D. McClenaghan, T. Buffeteau and J.-M. Vincent, *Chem. Commun.*, 2020, **56**, 8655–8658.
48 T. Narayanan, M. Sztucki, T. Zinn, J. Kieffer, A. Homs-Puron, J. Gorini, P. Van Vaerenbergh and P. Boesecke, *J. Appl. Cryst.*, 2022, **55**, 98–111.
49 P. Panine, M. Gradzielski and T. Narayanan, *Rev. Sci. Inst.*, 2003, **74**, 2451–2455.
50 The reader is refered to the following definition of a CT complex given in the IUPAC gold book (IUPAC. Compendium of Chemical Terminology, 2nd ed. Blackwell Scientific Publications, Oxford (1997).) ''An electron-donor–electron-acceptor complex, characterized by electronic transition(s) to an excited state in which there is a partial transfer of electronic charge from the donor to the acceptor moiety'' which implies that the complexation between the iodide donor and the viologen acceptor is revealed by new charge transfer band associated with the excitation of an electron from a largely Iodide-centered orbital to a largely viologen-centered orbital. The arrangement between the two species in space (side by side or stacked), however, remains to be established. Theoretical models are currently being developed to address this specific point.
51 M. Kumar Dixit, V. Kumar Pandey and M. Dubey, *Soft Matter.*, 2016, **12**, 3622–3630.
52 R. Yu, N. Lin, W. Yu and X. Y. Liu, *CrystEngComm*, 2015, **17**, 7986–8010.
53 X. Y. Liu and P. D. Sawant, *Adv. Mater.*, 2002, **14**, 421–426.
54 L. A. Feigin and D. I. Svergun, *Structure Analysis by Small-Angle X-Ray and Neutron Scattering*, Springer US, Boston, MA, 1987.
55 M. Mirzamani, A. Dawn, C. J. Garvey, L. He, H. Koerner and H. Kumari, *Phys. Chem. Chem. Phys.*, 2023, **25**, 131–141.
56 J. S. Pedersen and P. Schurtenberger, *Macromolecules*, 1996, **29**, 7602–7612.
57 R. A. Huggins, *Ionics*, 2002, **8**, 300–313.
58 C. Ho, I. D. Raistrick and R. A. Huggins, *J. Electrochem. Soc.*, 1980, **127**, 343–350.
59 J. Li, J. Xu, X. Li, W. Gao, L. Wang, L. Wu, M. Lee and W. Li, *Soft Matter*, 2016, **12**, 5572–5580.